W. Fundamenski, T. Eich, S. Devaux, S. Jachmich, S. Brezinsek, G. Maddison,
K. McCormick, G. Arnoux, M. Jakubowski, H. Thomsen, A. Huber, F. Militello,
E. Havlickova, D. Moulton and JET EFDA contributors

Multi-Parameter Scaling of Divertor Heat Load Profiles on JET and Implications for ITER

Multi-Parameter Scaling of Divertor Heat Load Profiles on JET and Implications for ITER

W. Fundamenski[1], T. Eich[2], S. Devaux[2], S. Jachmich[5], S. Brezinsek[4], G. Maddison[1], K. McCormick[2], G. Arnoux[1], M. Jakubowski[3], H. Thomsen[3], A. Huber[4], F. Militello[1], E. Havlickova[1], D. Moulton[6] and JET EFDA contributors*

JET-EFDA, Culham Science Centre, OX14 3DB, Abingdon, UK

[1]*EURATOM-CCFE Fusion Association, Culham Science Centre, OX14 3DB, Abingdon, OXON, UK*
[2]*Max-Planck Institut fur Plasmaphysik, IPP-Euratom Association, D-85748 Garching, Germany*
[3]*Max-Planck Institut fur Plasmaphysik, IPP-Euratom Association, Greifswald, Germany*
[4]*Institute fur Plasmaphysik, Forschungszentrum Julich GmbH, Euratom Association, TEC, D-52422, Julich, Germany*
[5]*Ecole Royale Militaire, Euratom Association, Belgium*
[6]*Imperial College of Science and Technology, London*
* See annex of F. Romanelli et al, "Overview of JET Results",
(Proc. 22 [nd] IAEA Fusion Energy Conference, Geneva, Switzerland (2008)).

ABSTRACT

Inter-ELM and ELM divertor heat loads were measured on JET in dedicated deuterium, hydrogen and helium discharges. Matched triplets (D, H, He) were obtained for different values of magnetic field, plasma current and heating power. In this article, the above experiments are described and the results are presented in terms of empirical scalings of inter-ELM and ELM wetted areas vs engineering parameters. The obtained inter-ELM scalings are then compared with those previously reported in the literature and with a wide range of theoretical predictions. Finally, implications for ITER are tentatively drawn, and a revised estimate for the power width in ITER is proposed.

1. INTRODUCTION

The key measurement of interest for tokamak power exhaust are the heat load profiles on the outer divertor target (which receives the majority of the average power). The physical mechanism determining these heat loads, both during the inter-ELM and the ELM phases, remains elusive [10]. One way of distinguishing between the various candidate mechanisms is to compare otherwise similar plasma discharges with different main ion mass and charge. In practice, such a comparison can be achieved for hydrogen (H; $A=1, Z=1$), deuterium (D; $A=2, Z=1$) and helium (He; $A=4, Z=2$) plasmas, the first two allowing the comparison of ion mass, the latter two of either mass or charge at constant $A/Z = 2$. By combining all three into a single comparison, the individual effect of A and Z on SOL energy transport can be inferred.

Needless to say, any conclusions drawn from such a study rest on the assumption that the same mechanism is dominant in all three types of plasmas, i.e. that the change in A and/or Z, does not change the dominant plasma dynamics. If it were to do so, e.g. if H plasmas were dominated by turbulent transport, and He plasmas by collisional transport, then any attempt to infer a physical model dominant in both plasmas would be doomed to failure. Thus, by undertaking such a study, we implicitly assume that such an outcome is highly unlikely, otherwise, the effort dedicated to the dedicated experiments and their analysis would be misspent. However, one should bear in mind that while unlikely, the possibility of such a multi-mechanism outcome is finite, and must be kept in mind when drawing conclusions and extrapolating the results to future devices, see section 4.3.

2. DESCRIPTION OF EXPERIMENTS

Recently, such a comparison was attempted at JET based on a series of dedicated experiments in H, D and He plasmas, with identical magnetic equilibria, i.e. poloidal plasma shapes. In each case, several engineering parameters were varied, albeit with limitations due to pumping and heating constraints in H and He plasmas: the toroidal magnetic field ($1T < B < 3T$), the plasma current ($1MA < I_p < 3MA$), and hence the edge safety factor ($3 < q_{95} < 5$), the neutral beam heating power ($2MW < P_{NBI} < 18MW$), the fuelling rate, Γ_0, and hence the line average electron density, n_e, and the corresponding Greenwald fraction ($0.5 < f_{GW} < 1$). From this extensive data set, roughly a dozen good comparison points between H, D and He were identified. Since many of the shots included

The key output of the experiment were the heat load profiles on the outer divertor target. These were calculated from the temperature evolution on the heat bearing septum replacement divertor plate (tile 5), which were measured using an infra-red camera with high spatial (< 2 mm along the target) and temporal (~ 80 μs) resolution, allowing separate measurement of inter-ELM, ELM, and time-averaged heat load profiles [5]. These profiles can be conveniently parametrized in terms of several derived quantities, as shown in Table 1. This includes the radial width of the heat load profile (which in this article will be expressed in terms of the *wetted area* - both inter-ELM and ELM - A_W [m^2]), the ELM *deposited energy* on tile 5, $E_{ELM,5}$ [kJ], the ELM *energy load*, ε_{ELM} [kJ/m^2], and the ELM *impact factor*, η_{ELM} [kJm^{-2}s$^{-1/2}$]. The notation, definitions and numerical calculation of these parameters are identical to those used in [14], and are reproduced below for convenience,

$$\varepsilon_{ELM}(R) = \int_{t_{start}}^{t_{end}} Q_{surf}(R,t)dt, \qquad E_{ELM} = 2\pi R \xi_{wet} \int_{R_{in}}^{R_{out}} \varepsilon_{ELM}(R)dR$$

$$A_W^{ELM} = \frac{E_{ELM}}{\varepsilon_{ELM}^{max}}, \qquad \eta_{ELM} = \frac{\varepsilon_{ELM}^{max}}{\sqrt{t_{dur}^{ELM}}} = \frac{E_{ELM}}{A_W^{ELM} \sqrt{t_{dur}^{ELM}}}$$

The wetted area is related to the integral width, $\lambda_q = \int Q(R)dR/Q_{max}$, by the expression,

$$A_W \sim 2\pi R \xi_{wet} \times \lambda_q \times FX, \tag{1}$$

where $R \sim 2.7$ m is the major radius and FX is the effective flux expansion (ratio of distances between flux surfaces along the outer target and the outer mid plane), with typically FX ~ 5.7 for tile 5 at 2.5 MA/2.5T; the factor $\xi_{wet} \sim 0.8$ represents the average toroidal wetted fraction, due to the toroidal inclination of the divertor tiles (fish scaling). Unless otherwise stated, all widths will be measured by distances mapped to the outer mid-plane.

3. RESULTS

3.1 DEUTERIUM PLASMAS

As initially observed on AUG [3], and more recently on JET [Devaux10, Eich10], the ELM heat load profiles are generally quite complex. To illustrate this complexity, which generally increases with relative ELM size, the inter-ELM, ELM and average heat load profiles are shown for three deuterium discharges with different relative ELM size, see Figure 1. We first note the apparent narrowness of the inter-ELM profiles, which have widths of ~4 mm mapped to the outer mid-plane, similar to the time averaged values previously reported in [9], based on thermocouple, Langmuir probe and (deconvoluted) infra-red profile measurements. Since the time averaged widths are only marginally broader than the inter-ELM ones (right frames), the agreement with previously reported

2

measurements would be expected.

We next observed the rapid rise of the ELM power load (left frames), which typically arrives on the ion transit time scale (typically sub-ms on JET). This rapid rise is also found in the far-SOL heat load (middle frames), which explains the broadening of the ELM-integrated profile. This broadening is not smooth but is rather characterized by distinct striations, which are generally interpreted as foot-prints of plasma filaments ejected during the ELM crash. The temporal evolution of these striations (typically ~ 10) has been studied elsewhere [2]. Their radial extent, and hence the width of the ELM heat load profiles, appears to increase with relative ELM size, up to $\lambda_q^{ELM} \sim 10$ mm for $\Delta W_{ELM}/W_{dia} \sim 9\%$, or 2.5 times broader than the inter-ELM value of ~ 4 mm.

It should be added that the above ELM behaviour differed substantially between small (mainly convective) ELMs and large (mainly conductive) ELMs: the former showing little or no ELM structure, movement of maximum heat load or broadening with respect to the inter-ELM profiles, while the latter showed significant ELM structure, broadening and movement of peak heat load. In general, the complexity of ELM heat load profiles, their average width and hence power delivered to the far-SOL and the limiters, increased with relative ELM size, as shown in Figure 1.

The measured increase of λ_q^{ELW} with ELM size is consistent with the observation that maximum temperature rise on the outer limiter, as measured by infra-red thermography, decreased with the outer gap (distance between separatrix and outer limiter) and increased roughly as the square root of the normalized (relative) ELM size, see Figure 2,

$$\Delta T/\Delta W_{ELM} \propto (\Delta W_{ELM}/W_{dia})^{\alpha}, \quad \alpha \sim 0.35 - 0.65, \tag{2}$$

where ΔT is the mean temperature rise of the limiter surface following ELM filament impact, ΔW_{ELM} is the energy released by the ELM, and W_{dia} is the plasma diamagnetic (stored) energy (roughly constant in these experiments). Hence, larger ELMs were found to deposit a larger fraction of their energy on the first wall, consistent with previous observations, and with divertor measurements [9]. It is worth making two observations in relation to these findings. First, the inferred value of the exponent $\alpha \sim 0.5$ is consistent the prediction of the interchange dominated filament motion [10]. Second, the radial decay length of the ELM energy load at the limiter appears to be roughly the same in the both cases with a value of ~ 20 mm, suggesting the difference in the effective ELM energy width occurs in the near-SOL rather than the far-SOL region [18].

3.2 DEUTERIUM-HYDROGEN-HELIUM COMPARISON

We next turn the analysis of dedicated D-H-He plasmas in identical magnetic geometry. The divertor heat load profiles for a matched D-H-He triplet with medium sized ELMs ($\Delta W_{ELM}/W_{dia} \sim 4\text{-}5\%$) are shown in Figure 3. We note that the inter-ELM profiles are marginally broader in H, and moderately broader in He, compared to the D plasma, with an associated reduction in the peak heat load (bottom frames). Since most of the power reaches the target during the inter-ELM phase,

the average profiles were similarly broadened. In contrast, the effect on ELM profiles was less pronounced, with comparable power width in D, H and He plasmas (bottom frames); as a result, the ratio of ELM to inter-ELM widths was smallest in He plasmas. The main difference in the ELM profiles between the three ion species, was the longer power arrival time (time difference from rise to peak of target heat load profile) in He compared, to either D or H (top frames), consistent with previous observations [17]. This increase in the time scale could be expected based on smaller sound speed (square root of mass and lower pedestal temperature and higher pedestal collisionality), as predicted by parallel kinetic modelling of the ELM pulse in the Scrape-off Layer [Tskhakaya06, Fundamensk06], which are in turn consistent with JET measurements [4].

Comparing the inter-ELM wetted areas for the entire database (12 D points, 6 H points and 6 He points), we find mean values of ~0.5 m2 for D and H, and ~0.6 m2 for He, see Figure 4. Due to an insufficient number of data points for H and He, a multi-variable regression is only meaningful for D data. The resulting fit,

$$A_W^{i\text{-}ELM,D} \propto B^{0.82\pm0.53} I_p^{-1.05\pm0.6} n^{-0.02\pm0.2} P^{0.02\pm0.15} \tag{3}$$

with an R^2 value (goodness of fit, not major radius) of 0.6, indicates the perennial inverse current dependence frequently reported on tokamaks, including JET [10]; the units of all quantities are the same as those shown in Table 1. This scaling is consistent, within its relatively large error bars, with that obtained using a much larger D only database [Eich11],

$$A_W^{i\text{-}ELM} \propto B^{0.4} I_p^{-1} P^{0.1} \propto B^{-0.6} q^1 P^{0.1}.$$

Combining data points for all three species, one finds a weaker B scaling (for constant I_p), a weak inverse A scaling, a square root Z scaling, consistent with broader inter-ELM profiles in He plasmas, Figure 5,

$$A_W^{i\text{-}ELM} \; [m^2] \sim 0.47 \times B^{0.45\pm0.20} I_p^{-0.77\pm0.24} n^{0.03\pm0.09} P^{0.09\pm0.06} A^{-0.03\pm0.07} Z^{0.22\pm0.11} \tag{4}$$
$$\sim 0.22 \times B^{-0.33\pm0.22} q_{95}^{0.78\pm0.24} n^{0.03\pm0.09} P^{0.09\pm0.06} A^{-0.03\pm0.07} Z^{0.22\pm0.11}$$

which once again is consistent (within the error bars) with that found using the larger D database [Eich11]. The above scaling has an R^2 value of 0.67 and a standard deviation of 0.11, and thus offers a statistically meaningful, albeit still poor, fit to the overall underlying data. In view of the small number of data points, the errors on selected exponents are quite large. With this in mind, we can determine no meaningful mass dependence, and only a small positive charge dependence, on the inter-ELM wetted area, i.e. little change between H and D, and a small increase from D to He. These mass and charge dependencies are much weaker than those found in earlier measurements on

4

JET in D and He plasmas, where a somewhat stronger broadening of the total (time average over both inter-ELM and ELM phases) wetted area was observed [Fundamenski05],

$$A_W{}^{total} \propto B^{-1.0} q_{95}{}^{0.6} P^{-0.4} n^{0.25} A^{\alpha} Z^{\beta}, \qquad \alpha + \beta \sim 1 \tag{5}$$

Due to the limitations of the diagnostic techniques, a distinction between the inter-ELM and ELM phases could not be drawn in the earlier experiments; moreover since only D and He plasmas were compared, only the sum of the A and Z exponents could be inferred. Finally, the field, current, power and density exponents in the newly obtained $A_W{}^{i\text{-ELM}}$ scaling, (4), are also broadly consistent with those obtained using the much larger D only database from recent JET experiments [Eich11].

We next consider the ELM heat load profiles. The ELM wetted area, energy load and the impact factor, for an average (mean) ELM over 1-2 sec interval around each data point (D, H and He) are plotted vs the ELM deposited energy, Figure 6, and vs the deposited energy normalized by the plasma stored energy, Figure 7 (note that with an inner-outer asymmetry of 2:1, we have $E_{ELM,5} \sim \Delta W_{ELM}/3$). We note that the ELMs are relatively small, with $E_{ELM},5 \sim \Delta W_{ELM}/3 < 60$ kJ, $E_{ELM,5}/W_{dia} \sim 1\%$, $\Delta W_{ELM}/W_{dia} \sim 3\%$ and $\Delta W_{ELM}/W_{ped} \sim 10\%$. In this range, the ELM wetted area is between 0.7 and 1.3 m^2, is only a weak function of ELM energy and is similar for D, H and He. The ELM energy load is less than 60 kJ/m^2, increases roughly linearly with ELM size, and is again comparable for D, H and He. Finally, the maximum ELM impact factor also increases with ELM size, but for $E_{ELM,5} > 25$ kJ, becomes smaller for He than for D or H; this saturation appears to be caused not by a larger wetted area, but by a longer ELM duration, as shown in the lower right frame in Figure 6 and 7. Overall, these four quantities are better ordered by the absolute, rather than relative, ELM size, i.e. Figure 6 rather than Figure 7. This suggests the presence of hidden variables (current, field, heating power, fuelling rate, hence pedestal conditions, and A & Z) which influence these ELM heat load quantities.

Finally, we examine the combined D-H-He data for ELM wetted areas plotted vs the best-fit power law scaling, see Figure 5 (left frame),

$$
\begin{aligned}
A_W{}^{ELM} &\sim 0.6 \times B^{0.11 \pm 0.45} I_p{}^{-0.48 \pm 0.52} n^{0.21 \pm 0.21} P^{0.17 \pm 0.13} E_{ELM,5}{}^{0.01 \pm 0.05} A^{-0.05 \pm 0.17} Z^{0.02 \pm 0.25} \\
&\propto B^{-0.37 \pm 0.45} q_{95}{}^{0.48 \pm 0.52} n^{0.21 \pm 0.21} P^{0.17 \pm 0.13} E_{ELM,5}{}^{0.01 \pm 0.05} A^{-0.05 \pm 0.17} Z^{0.02 \pm 0.25}
\end{aligned}
\tag{6}
$$

This expression has an R^2 value of 0.16 and a standard deviation of 0.19, and thus offers only a very poor fit to the underlying data, with the error on all exponents comparable to the exponent value, suggesting the presence of additional (hidden) variables which determine the ELM wetted area. Specifically, we can determine only a negligible mass and charge dependences on the ELM wetted area, in contrast to the inter-ELM area, where the meaningful charge dependence was inferred. It is also interesting to note that the wetted area does not seem to increase with the ELM size (amplitude), which seems to contradict the evident scaling with ELM size in Figure 1, and reported elsewhere [Devaux10, Eich10]. We will return to the point in due course.

Bearing in mind the associated errors, we next compare the inter-ELM and ELM scalings (4) and (6). We thus find virtually the same B and A scalings, but a somewhat weaker q_{95} (or connection length, $L_{\parallel} \sim \pi q_{95}R$) and Z scalings. Figure 6 also shows the ratio of inter-ELM vs ELM wetted areas, (the inverse of the degree of profile broadening), which following an independent regression is found to scale as

$$A_W^{i\text{-}ELM}/A_W^{ELM} \sim 0.77 \times B^{0.33\pm0.42}I_p^{-0.3\pm0.49}n^{-0.176\pm0.2}P^{-0.08\pm0.12}E_{ELM,5}^{-0.01\pm0.05}A^{0.02\pm0.16}Z^{0.25\pm0.24} \quad (7)$$

with an R^2 value of 0.48 and standard deviation of 0.2, i.e. offering only a poor fit to the data. Within the error bars, we observe only a weak positive dependence on Z, and possible a weak positive dependence on q. Hence, on average, the degree of broadening is ~20% larger in D and H, than in He, for comparable plasma conditions, see Figure 4.

Similarly, one can construct regression fits for the ELM energy load, ε_{ELM}, ELM impact factor, η_{ELM}, and ELM heat impulse width, τ_{ELM}. These three scalings are shown as equations (8), (9) and (10) below. We discuss each in turn.

The ELM energy load, εELM, is found to scale as

$$\varepsilon_{ELM} \propto B^{0.56\pm0.75}I_p^{-0.01\pm0.87}n^{0.63\pm0.35}P^{-0.16\pm0.22}E_{ELM,5}^{0.26\pm0.08}A^{-0.28\pm0.28}Z^{0.32\pm0.42} \quad (8)$$

with an R2 value of 0.85 and a standard deviation/error of 0.29, thus offering a reasonable fit to the underlying data. One observes a statistically meaningful scaling with ELM energy, with an exponent of roughly 0.25, but only negligible scalings with both mass or charge (errors larger than exponents). Since εELM = EELM,5 /AWELM, expression (8) seems to imply that the ELM wetted area should increase with ELM size with an exponent of 1-0.26 ~ 0.74, i.e.,

$$A_W^{ELM} \propto E_{ELM,5}^{0.74\pm0.08}, \quad (9)$$

in contrast to the direct regression of A_W^{ELM} in which only a moderate dependence on ELM size was found. The reason for this discrepancy is likely to lie in the poor quality of the regression (6), as evident by a low R^2 value. Since the R^2 of regression (8) is substantially higher, this suggests that the ELM size scaling in (9) is more accurate that that in (6). This conclusion would be consistent with the tendency of ELM wetted area to increase with ELM size as reported elsewhere [Devaux10, Eich10], and evident in Figures 1 and 2.

The ELM impact factor, ηELM, is found to scale as

$$\eta_{ELM} \, \varepsilon \, B^{0.24\pm0.59}I_p^{-0.24\pm0.69}n^{0.85\pm0.27}P^{0.29\pm0.17}E_{ELM,5}^{0.2\pm0.06}A^{-0.33\pm0.22}Z^{-0.23\pm0.33} \quad (10)$$

6

with an R2 value of 0.91 and a standard deviation/error of 0.23, thus offering a good fit to the underlying data. The dominant scaling is that with the line average density. In addition, we again observe a statistically meaningful scaling with ELM energy, with an exponent of roughly 0.2, and negligible scalings with ion mass and charge. This latter effect can be traced to the dependence on the length of the ELM impulse as observed at the target which in turn is found to scale as

$$\tau_{ELM} \propto B^{1.05\pm2.06} I_p^{0.1\pm2.54} n^{-0.09\pm1.0} P^{1.45\pm0.65} E_{ELM,5}^{0.04\pm0.24} A^{-0.29\pm0.84} Z^{1.44\pm1.29} \qquad (11)$$

with an R^2 value of 0.42 and a standard deviation/error of 0.38, i.e. a rather poor fit to the underlying data. With this caveat, one does observe a strong charge dependence, indicating that ELM pulses in He plasmas are much broader in time (longer dureation) that those in D or H plasmas, consistent with the scaling of η_{ELM} with Z in (10).

4. INTERPRETATION OF THE INTER-ELM POWER WIDTH SCALING

As is evident from Figure 1 and 3, the time average profiles and inter-ELM heat load profiles are comparable, due to the fact that most of the power is removed from the plasma during the inter-ELM phase. We may thus expect the average profiles to act as a proxy for the inter-ELM profiles, which were measured previously. Despite these arguments, we find that the wetted area scalings (3) and (4) differ from that reported for time-averaged heat load profiles of natural density, high power H-modes [9], $\lambda_q^{ave} \propto B^{-1} q_{95}^{0.6} P^{-0.4} n^{0.2}$, see equation (5). This discrepancy could be ascribed to a number of factors such as the differences in the diagnostic technique, the magnetic configuration and flux expansion between the past and present experiments, as well as the relative scarcity of high power shots data in the present data set.

From among these factors, the differences in the diagnostic techniques offer the most likely explanation, since the earlier diagnostic technique (made with the vertically swept thermocouple technique [Riccardo03]), measured time-averaged heat load profiles, while the latter yield separate profiles for the inter-ELM and ELM phases. Since the wetted areas during these two phases are observed to scale differently, see equation (7), specifically the AwELM scaling with ELM size, and the AWi-ELM scaling with Z, the ELM averaged measurement of AW does not (by itself) represent a good estimate of either the inter-ELM or the ELM wetted areas (this point was recently documented based on JET data in [5]).

4.1 DERIVATION OF THEORETICAL ESTIMATES OF THE POWER WIDTH SCALING

In order to interpret the inter-ELM results, it is useful to construct a simple model of SOL power exhaust during this phase, from which the wetted area (and/or power width) could be derived. We outline one such construction below, obtaining several families of models for λ_q , and deriving their scaling with field, current, power, density, mass and charge, which can then be compared to experimental results.

We begin with a simple expression of the SOL power width, based on a competition between perpendicular and parallel transport. Specifically, we assume radial advection with velocity $V_\perp$ and parallel losses to the target with removal time $\tau_\parallel$. The power width can then be written simply as [10],

$$\lambda_q \sim V_\perp \tau_\parallel$$

While the limitations of such a simplified approach should be self-evident (reduction of a 3-D/2-D problem to a 0-D expression), we feel these are outweighed by its key merits of simplicity and ease-of-use. Moreover, a comparison of the simple (0-D) approach against 2-D simulations using the EDGE2D/NIMBUS code have shown a surprising level of agreement between the two [16], reinforcing the case for the former, especially when only tendencies (scalings) rather than absolute magnitudes are predicted and compared.

The parallel removal time can be estimated by making two asymptotic assumptions about parallel transport, namely dominance of (ion) convection or (electron) conduction:

Model 1: (ion) convection dominates: $\tau_\parallel \sim L_\parallel / c_s$

Model 2: (electron) conduction dominates: $\tau_\parallel \sim L_\parallel^2 / \chi_{\parallel e}$

where $L_\parallel \sim \pi q R$ is the parallel connection length in the SOL, $c_s \sim \sqrt{(ZT_e + T_i)/m_i} \sim \sqrt{(Z+1)T/Am_p} \propto Z^{1/4}T^{1/2}A^{-1/2}$ is the plasma sound speed, and ($\chi_{\parallel e} \propto T_e^{5/2} n_e Z^{1/2}$ is the parallel electron heat diffusivity [Braginskii65]; note that we assumed that $T_e \sim T_i$ and that Z only varies between 1 and 2 (H & D versus He), so that $(Z + 1) \propto Z^{1/2}$.

The radial velocity can be estimated by making several plausible assumptions about perpendicular transport, as outlined below:

Model A : ion-ion (collisional) heat diffusion: $V_\perp \sim \sqrt{\chi_{\perp i}^{ci} \tau_\parallel}$

Model B : Drift ordered (Gyro-Bohm) velocity: $V_\perp \sim \delta c_s \sim c_s(\rho_s / \lambda_q)$

Model C: Transport ordered velocity: $V_\perp \sim \delta^2 c_s \sim c_s(\rho_s / \lambda_q)^2$

Model D : Curvature GC-drift velocity: $V_\perp \sim c_s(\rho_s / R)$

Model E : Interchange radial velocity: $V_\perp \sim c_s\sqrt{\rho_s / R}$

where $\rho_s = c_s / \Omega_i \propto T^{1/2} B^{-1} A^{1/2} Z^{-3/4}$ is the ion gyro-radius at the plasma sound speed, $\cdot\delta = \rho_s/L_p \sim \rho_s/\lambda_q$ is the plasma magnetization, R is the tokamak major radius, $\chi_{\perp i}^{ci} \sim \rho_i^2 \nu_{\perp i} \sim T^{-1/2} n_i B^{-2} Z^2 A^{-1/2} \sim T^{-1/2} n_e B^{-2} Z A^{-1/2}$ is the classical ion perpendicular heat diffusivity, and $\nu_i \sim T^{-3/2} n_i Z^4 A^{-1/2} \sim T^{-3/2} n_e Z^2 Z A^{-1/2}$ is the ion-ion collision frequency [13]. Here and below we will assume quasi-neutrality $n \equiv n_e = Zn_i$ and write all expressions in terms of the electron density. In the expression for the interchange velocity, which follows from, $V_\perp \sim c_s \sqrt{(\Delta p/p)(I/R)}$ we assumed that $\Delta \rho/\rho \sim const$ and that $l \sim \rho_s$, i.e. that the (blob) structure size inside the ETB is of the order of the gyro-radius, rather than of the larger meso-scale, $\sqrt{\rho_s/\lambda_q}$ pertinent to the turbulent (L-mode) edge.

In the above expressions, we used the plasma sound speed cs as the characteristic (ion) fluid velocity, entering both parallel convection in models 1 (via $L_\parallel /c_s$) and radial drifts in models B to E, via c_s and $\rho_s = c_s / \Omega i$. Alternatively, we could have chosen the ion thermal velocity in these expressions. We will label models in which $v_{ti} \sim T_i / m_i \propto T^{-1/2} A^{-1/2}$ replaces $c_s \sim \sqrt{(ZT_e + T_i)/m_i} \propto Z^{1/4} T^{1/2} A^{-1/2}$ by an asterix, i.e.

Model B*:	Drift ordered (Gyro-Bohm) velocity:	$V_\perp \sim \delta v_{ti} \sim v_{ti}(\rho_i / \lambda_q)$
Model C*:	Transport ordered velocity:	$V_\perp \sim \delta^2 v_{ti} \sim v_{ti}(\rho_i / \lambda_q)^2$
Model D*:	Curvature GC-drift velocity:	$V_\perp \sim v_{ti}(\rho_i / R)$
Model E*:	Interchange drive radial velocity:	$V_\perp \sim v_{ti}\sqrt{\rho_i / R}$

Combining the parallel and perpendicular assumptions, one finds 2 x 9 models for the power width. Denoting each model by two symbols, the first denoting the parallel and the second the perpendicular assumption, we find the following scalings,

Model 1A:	$\lambda_q \propto B^{-1} (qR)^{1/2} T^{-1/2} n^{1/2} A^{1/2} Z^{3/8} \propto a B^{-1/2} I_p^{-1/2} T^{-1/2} n^{1/2} A^{1/2} Z^{3/8}$
Model 1B:	$\lambda_q \propto B^{-1/2} (qR)^{1/2} T^{1/4} n^0 A^{1/4} Z^{-3/8} \propto a I_p^{-1/2} T^{1/4} n^0 A^{1/4} Z^{-3/8}$
Model 1C	$\lambda_q \propto B^{-2/3} q^{1/3} R^{1/3} T^{1/3} n^0 A^{1/3} Z^{-1/2} \propto a^{2/3} \varepsilon^0 B^{-1/3} I_p^{-1/3} T^{1/3} n^0 A^{1/3} Z^{-1/2}$
Model 1D:	$\lambda_q \propto B^{-1} q T^{1/2} n^0 A^{1/2} Z^{-3/4} \propto a \varepsilon I_p^{-1} T^{1/2} n^0 A^{1/2} Z^{-3/4}$
Model 1E:	$\lambda_q \propto B^{-1/2} q R^{1/2} T^{1/4} n^0 A^{1/4} Z^{-3/8} \propto a^{3/2} \varepsilon^{1/2} B^{1/2} I_p^{-1} T^{1/4} n^0 A^{1/4} Z^{-3/8}$
Model 1B*:	$\lambda_q \propto B^{-1/2} (qR)^{1/2} T^{1/4} n^0 A^{1/4} Z^{-1/2} \propto a I_p^{-1/2} T^{1/4} n^0 A^{1/4} Z^{-1/2}$
Model 1C*:	$\lambda_q \propto B^{-2/3} q^{1/3} R^{1/3} T^{1/3} n^0 A^{1/3} Z^{-2/3} \propto a^{2/3} \varepsilon^0 B^{-1/3} I_p^{-1/3} T^{1/3} n^0 A^{1/3} Z^{-2/3}$
Model 1D*:	$\lambda_q \propto B^{-1} q T^{1/2} n^0 A^{1/2} Z^{-1} \propto a \varepsilon I_p^{-1} T^{1/2} n^0 A^{1/2} Z^{-1}$
Model 1E*:	$\lambda_q \propto B^{-1/2} q R^{1/2} T^{1/4} n^0 A^{1/4} Z^{-1/2} \propto a^{3/2} \varepsilon^{1/2} B^{1/2} I_p^{-1} T^{1/4} n^0 A^{1/4} Z^{-1/2}$
Model 2A:	$\lambda_q \propto B^{-1} (qR) n T^{-3/2} A^{1/4} Z^1 \propto a^2 I_p^{-1} n T^{-3/2} A^{1/4} Z^1$
Model 2B:	$\lambda_q \propto B^{-1/2} (qR) T^{-3/4} n^{1/2} A^0 Z^{1/4} \propto a^2 B^{1/2} I_p^{-1} T^{-3/4} n^{1/2} A^0 Z^{1/4}$
Model 2C	$\lambda_q \propto B^{-2/3} q^{2/3} R^{2/3} T^{-1/3} n^{1/3} A^{1/6} Z^{-1/12} \propto a^{4/3} \varepsilon^0 B^0 I_p^{-2/3} T^{-1/3} n^{1/3} A^{-1/6} Z^{-1/12}$
Model 2D:	$\lambda_q \propto B^{-1} q^2 R T^{-3/2} n A^0 Z^{1/2} \propto a^3 \varepsilon B I_p^{-2} T^{-3/2} n A^0 Z^{1/2}$
Model 2E:	$\lambda_q \propto B^{-1/2} q^2 R^{3/2} T^{-7/4} n A^{-1/4} Z^{7/8} \propto a^{7/2} \varepsilon^{1/2} B^{3/2} I_p^{-2} T^{-7/4} n A^{-1/4} Z^{7/8}$
Model 2B*:	$\lambda_q \propto B^{-1/2} (qR) T^{-3/4} n^{1/2} A^0 Z^0 \propto a^2 B^{1/2} I_p^{-1} T^{-3/4} n^{1/2} A^0 Z^0$
Model 2C*:	$\lambda_q \propto B^{-2/3} q^{2/3} R^{2/3} T^{-1/3} n^{1/3} A^{1/6} Z^{-1/3} \propto a^{4/3} \varepsilon^0 B^0 I_p^{-2/3} T^{-1/3} n^{1/3} A^{-1/6} Z^{-1/3}$
Model 2D*:	$\lambda_q \propto B^{-1} q^2 R T^{-3/2} n A^0 Z^0 \propto a^3 \varepsilon B I_p^{-2} T^{-3/2} n A^0 Z^0$
Model 2E*:	$\lambda_q \propto B^{-1/2} q^2 R^{3/2} T^{-7/4} n A^{-1/4} Z^{1/2} \propto a^{7/2} \varepsilon^{1/2} B^{3/2} I_p^{-2} T^{-7/4} n A^{-1/4} Z^{1/2}$

In the above expressions, the first form expresses the current dependence in terms of the safety factor, q, and the second in terms of the plasma current, I_p; here we used the approximate expression $q = \varepsilon B/B_p \propto = a\varepsilon B/I_p$,where $\varepsilon = a/R$ is the inverse tokamak aspect ratio and   is the poloidal field at the edge.

Since in the experiment, it is the input power, P, rather than the separatrix temperature, T, that is held constant, we need to introduce an estimate for T in terms of P and other variables. The two expressions corresponding to models 1 and 2 are given below,

Model 1:   (ion) convection dominates: $T_u \sim \left(\dfrac{Pq}{\lambda_q R \varepsilon n_e}\right)^{2/3}$

Model 2:   (electron) conduction dominates: $T_u \sim \left(\dfrac{Pq^2 Z}{\lambda_q \varepsilon}\right)^{2/7}$

The first expression corresponds to the sheath limited SOL, and the latter to the conduction limited SOL [Stangeby00]. Inserting these into our previous model scalings, we find

Model 1A: $\lambda_q \propto B^{-3/2} q^{1/4} \varepsilon^{1/2} R^{5/4} P^{-1/2} n^{5/4} A^{3/4} Z^{9/16}$

Model 1B: $\lambda_q \propto B^{-3/7} q^{4/7} \varepsilon^{-1/7} R^{2/7} P^{1/7} n^{-1/7} A^{3/14} Z^{-9/28}$

Model 1C: $\lambda_q \propto B^{-6/11} q^{5/11} \varepsilon^{-2/11} R^{1/11} P^{2/11} n^{-2/11} A^{3/11} Z^{-9/22}$

Model 1D: $\lambda_q \propto B^{-3/4} q^{1} \varepsilon^{-1/4} R^{-1/4} P^{1/4} n^{-1/4} A^{3/8} Z^{-9/16}$

Model 1E: $\lambda_q \propto B^{-3/7} q^{1} \varepsilon^{-1/7} R^{2/7} P^{1/7} n^{-1/7} A^{3/14} Z^{-9/28}$

Model 1B*: $\lambda_q \propto B^{-3/7} q^{4/7} \varepsilon^{-1/7} R^{2/7} P^{1/7} n^{-1/7} A^{3/14} Z^{-3/7}$

Model 1C*: $\lambda_q \propto B^{-6/11} q^{5/11} \varepsilon^{-2/11} R^{1/11} P^{2/11} n^{-2/11} A^{3/11} Z^{-18/33}$

Model 1D*: $\lambda_q \propto B^{-3/4} q^{1} \varepsilon^{-1/4} R^{-1/4} P^{1/4} n^{-1/4} A^{3/8} Z^{-3/4}$

Model 1E*: $\lambda_q \propto B^{-3/7} q^{1} \varepsilon^{-1/7} R^{2/7} P^{1/7} n^{-1/7} A^{3/14} Z^{-3/7}$

Model 2A: $\lambda_q \propto B^{-7/4} q^{1/4} \varepsilon^{3/4} R^{7/4} P^{-3/4} n^{7/4} A^{7/16} Z^{1}$

Model 2B: $\lambda_q \propto B^{-7/11} q^{8/11} \varepsilon^{3/11} R^{14/11} P^{-3/11} n^{7/11} A^{0} Z^{1/22}$

Model 2C: $\lambda_q \propto B^{-14/19} q^{10/19} \varepsilon^{1/6} R^{14/19} P^{-2/19} n^{7/19} A^{7/38} Z^{-45/228}$

Model 2D: $\lambda_q \propto B^{-7/4} q^{2} \varepsilon^{3/4} R^{7/4} P^{-3/4} n^{7/4} A^{0} Z^{1/8}$

Model 2E: $\lambda_q \propto B^{-1} q^{2} \varepsilon^{1} R^{3} P^{-1} n^{2} A^{-1/2} Z^{3/4}$

Model 2B*: $\lambda_q \propto B^{-7/11} q^{8/11} \varepsilon^{3/11} R^{14/11} P^{-3/11} n^{7/11} A^{0} Z^{-3/11}$

Model 2C*: $\lambda_q \propto B^{-14/19} q^{10/19} \varepsilon^{1/6} R^{14/19} P^{-2/19} n^{7/19} A^{7/38} Z^{-9/19}$

Model 2D*: $\lambda_q \propto B^{-7/4} q^{2} \varepsilon^{3/4} R^{7/4} P^{-3/4} n^{7/4} A^{0} Z^{-3/4}$

Model 2E*: $\lambda_q \propto B^{-1} q^{2} \varepsilon^{1} R^{3} P^{-1} n^{2} A^{-1/2} Z^{0}$

While it appears contradictory with the starting assumptions in models 1 and 2, it has been suggested, that it may be possible that the upstream (ion and electron) temperature is always determined by parallel electron conduction, even in the case of model 1, where we assume that parallel ion convection dominates ion transport. Without a deeper investigation of the physical mechanisms which would lead to such an eventuality, (e.g. the degree of near-SOL B-field stochasticity), it is not possible to decide on the physical admissibility of such models. For completeness, we derive the power width scalings corresponding to this assumption, denoting the models with a plus '+' sign.

Model 1A+: $\lambda_q \propto B^{-7/6} \, q^{1/4} \, \varepsilon^{1/6} \, R^{7/12} \, P^{-1/6} \, n^{7/12} \, A^{7/12} \, Z^{0.271}$

Model 1B+: $\lambda_q \propto B^{-7/15} \, q^{3/5} \, \varepsilon^{-1/15} \, R^{7/15} \, P^{1/15} \, n^0 \, A^{7/30} \, Z^{-17/60}$

Model 1C+: $\lambda_q \propto B^{-14/23} \, q^{11/23} \, \varepsilon^{-2/23} \, R^{7/23} \, P^{2/23} \, n^0 \, A^{7/23} \, Z^{-17/46}$

Model 1D+: $\lambda_q \propto B^{-7/8} \, q^{9/8} \, \varepsilon^{-1/8} \, R^0 \, P^{1/8} \, n^{-1/4} \, A^{7/16} \, Z^{-17/32}$

Model 1E+: $\lambda_q \propto B^{-7/15} \, q^{16/15} \, \varepsilon^{-1/15} \, R^{7/15} \, P^{1/15} \, n^0 \, A^{7/30} \, Z^{-17/60}$

Finally, it is appropriate to mention a number of 'non-transport' models which are occasionally used to estimate the power width in the SOL. The first is the ion gyro-radius itself, which acts as a natural measure of radial plasma extent and leads to the scalings,

Model 3: Hybrid gyro-radius, $\lambda_q \propto \rho_s = c_s / \Omega_i \propto T^{1/2} B^{-1} A^{1/2} Z^{-3/4}$

$\lambda_q \propto B^{-7/8} \, q^{1/4} \, \varepsilon^0 \, R^0 \, P^{1/15} \, n^0 \, A^{7/16} \, Z^{-17/32}$

Model 3*: Ion gyro-radius, $\lambda_q \propto \rho_i = v_{ti} / \Omega_i \propto T^{1/2} B^{-1} A^{1/2} Z^{-1}$

$\lambda_q \propto B^{-7/8} \, q^{1/4} \, \varepsilon^0 \, R^0 \, P^{1/15} \, n^0 \, A^{7/16} \, Z^{-25/32}$

The second are pressure gradient lengths for marginal stability against interchange modes, ideal ballooning modes and interchange turbulence [12, Scott02]. While these lengths are strictly valid only on closed field lines, and hence inside the separatrix, there is some evidence to suggest that they may influence the near-SOL power width profiles: (i) it is observed that the radial derivative of the plasma pressure profiles is continous across the separatrix, i.e. there is little empirical evidence for a step change in the radial gradient of the pressure, (ii) it is generally accepted that the edge transport barrier extends marginally outside the separatrix. While the link between upstream pressure profile and target heat load profiles is far from clear and depends on divertor conditions, e.g. [1], it has been occasionally suggested that this link offers the best route to estimating the heat load profiles in future devices (indeed, the standard ITER estimate of the power width was obtained using such a stability argument, model 4b below). Finally, a relation between upstream pressure gradient and interchange/ballooning instabilities was clearly established on Alcator C-mod, [15].

The interchange mode estimate follows from the Mercier criterion for large q, $\alpha\varepsilon/s^2 \sim$ cons, the ideal ballooning mode estimate from the first stability criterion, and $\alpha/s^2 \sim q^3 \beta'/\varepsilon q' \sim 0.6$ cons the interchange turbulence estimate from $\beta \sim \beta \, (L_\parallel/L_\perp)^2 \sim \beta \, (qR/Lp)^2$. In the above $\alpha = -q^2 R \beta'$ is the ballooning parameter, $s = aq'/q$ is the m̂agnetic shear at the edge, L_p is the pressure gradient length, and primer denotes a radial derivative. Assuming that $\lambda_q \sim L_p$ as obtained from above, that the edge beta scales roughly as the Troyon beta limit, $\beta \propto \varepsilon/q$, and that $dq/dr \sim q/a$, so that $s \sim$ constant, one finds

Model 4a: Interchange limit, $\lambda_q \propto a \, \varepsilon \, q^2 \, \beta \sim q \, a \, \varepsilon^2$

Model 4b: Ideal ballooning limit, $\lambda_q \propto q^2 \, R \, \beta \propto q \, a$

Model 4c: Turbulent interchange limit, $\lambda_q \propto q \, R \, \beta^{1/2} \sim q^{1/2} \, R \, \varepsilon^{1/2}$

with no dependence on magnetic field, power, density, and ion mass or charge.

4.2 Comparison between models and experiment

Figures 7 and 8 show a comparison of all the above model predictions with the inferred A and Z scaling for the inter-ELM phase of JET discharges, i.e. $\lambda q \propto A^{-0.03\pm0.07}Z^{0.22\pm0.11}$, the former as a scatter plot of the exponents and the latter in terms of the root-mean-square error between the predicted and measured exponents. Although in the experiment, the input power, P, rather than the separatrix temperature, T, were held constant, the figure shown the comparison with exponents of both constant T and P predictions. Only two models (at constant SOL power) agree with the experimental result within the indicated error bars of the inferred exponents, namely model 2D (electron conduction + curvature drift); just outside the allowed range, but in close proximity is model 2B (electron conduction + drift ordered velocity) and models 4a-c (the interchange/ballooning marginal stability), which have negligible A & Z scaling. Since models 2B and 2D include a combination of parallel electron conduction and perpendicular convection with some form of the drift-ordered velocity, this result suggests that these mechanisms likely dominate near-SOL transport during the inter-ELM phase of JET D, H, and He plasmas (assuming of course that the same mechanism is indeed dominant for the three ions species plasmas). The other alternative, would be marginal stability to interchange/ballooning modes, models 4a to 4c. In view of the good match in other plasma quantities (D-H-He triple approach) and hence the small error bar on the A and Z exponents, the above result offers a strong evidence against the many other models which do not agree with the measured A & Z scaling.

It is worth noting that these conclusions are in contradiction to that reached previously [Fundamenski05] based on a measurement of time average heat load widths in D and He plasmas (no H plasmas available). This allowed the determination of the sum of A and Z exponents in the time average width scaling, $\lambda_q \propto A^\alpha Z^\beta$ as $\alpha + \beta \sim 1$. This relationship, shown as the line in Figure 8, is indeed best matched by models 1A and 2A, i.e. by radial transport dominated by classical ion conduction, consistent with conclusions in [Fundamenski05].

We next compare the predicted and measured scalings of the other variables, excluding the A and Z scalings (as well as the size and aspect ratio, these being constant on a single machine), and the density dependence, which is the weakest link in the comparison (recall that the empirical scaling was obtained in terms of the line average density, while the density entering the models is the separatrix density, which depends on the height of the density pedestal, and hence on field, current, etc.), as a proxy of the results from only D plasmas. The resulting errors between predicted and measured exponents are shown in Figure 9. It is clear that a wide range of models are consistent with the available data within the experimental error bar of ~0.25 (calculated as the root mean square error on the individual exponents). In particular, models 1B, 1C, 1D, 1E (and their variants * and +), 2B, 2C, 4a, 4b 4c are all consistent with observations. In contrast, models 1A, 2A, 2D, 2E are in gross disagreement with measurements.

Finally, we examine the agreement with all the variables, with the exception of size, aspect ratio and density. The results, shown in Figure 10 in terms of the root-mean-square error between the predicted and measured exponents, indicates that model 2B – combination of parallel electron

conduction and drift-ordered (Gyro-Bohm) perpendicular velocity – offers the best overall fit to the data, followed closely by models 4a & 4b (marginal stability to ideal interchange & ballooning modes). This would suggest that radial transport in the near-SOL is dominated by residual levels of turbulence in the edge transport barrier region, especially if this turbulence is driven mainly by pressure driven (ballooning) modes. These results should be tested further by comparison with additional JET scalings based on the extensive D only data set, although as we reported earliers, these results are broadly consistent with those obtained from a composite of D, H and He plasmas. More importantly, the JET results should be combined with those from other devices in order to establish a size and aspect ratio dependence, and thereby distinguish between the optimal model(s).

4.3 Extrapolation to ITER

Based on the above findings, it is possible to attempt a prediction of the inter-ELM power width on ITER, in two different ways. First, we extrapolate directly from JET empirical data, equation (4),

$$A_W^{\text{i-ELM}} \; [m^2] \sim 0.22 \times B^{-0.33} q_{95}^{0.78} n^{0.03} P^{0.09} A^{-0.03} Z^{0.22}$$

from which we obtain the expression for the integral power width n JET,

$$\lambda_q^{\text{i-ELM}} \; [mm] = 2.85 \times B^{-0.33} q_{95}^{0.78} n^{0.03} P^{0.09} A^{-0.03} Z^{0.22}$$

This scaling needs to be combined with an assumed size dependence, which is absent from the above expression (derived from a single machine, and hence for R = const). For this purpose, we adopt the size dependence of the best-fit model 2B, i.e. $\lambda_q \propto R^{14/11}$ (noting that a similar scaling follows from second best model 4b-c, $\lambda_q \propto R$), and adopt the ratio of ITER and JET major radii as 6m / 3m ~ 2. Inserting the approximate ITER values,

$$B \sim 5.2T, \;\; q_{95} \sim 3, \;\; n_{ped} \sim 6x10^{19} \, m^{-3}, \;\; P = 120 \, MW,$$

into the JET expression for $\lambda_q^{\text{i-ELM}}$ and multiplying by $2^{14/11} \sim 2.4$, yields an expression of the ITER power width of $\lambda_q^{\text{i-ELM}} \sim 6.7mm$ for D & H, and $\lambda_q \sim 7.6mm$ for He (or $\lambda_q^{\text{i-ELM}} \sim 5.5 \, mm$ for D & H, and $\lambda_q^{\text{i-ELM}} \sim 6.3mm$ for He assuming the linear size scaling implied by models 4a-c), which are somewhat higher than the standard ITER assumption of 5mm.

As a word of caution, it should be stressed that the above predictions would be reduced if a weaker size dependence was assumed. Examining those models with adequate agreement to D only data, namely convective models 1B to 1E+, and conductive models 2B to 2C*, and stability models, 4b and 4c, see Figure 10, we find that their size dependence ranges from $R^{-1/4}$ for models 1D and 1D* to $R^{14/11}$ for models 2B and 2B*. Thus, model 2B offers the largest likely size scaling, and hence an upper estimate consistent with D only data. If we were to adopt the weakest size dependence (model 1D), $\lambda_q \propto R^{-1/4}$, the above estimates would be reduced by a factor of $2^{3/2} \sim 2.8$, giving a value of only 2.4 mm for D plasmas! While these models are clearly inconsistent with the A and Z scaling observed on JET, one cannot rule out the fairly remote possibility that SOL transport in D

plasmas is in fact dominated by a different physical mechanism than in H and/or He plasmas (recall our proviso in the introduction), thus introducing a small, but finite, downside risk to the standard ITER estimate of 5 mm. This risk offers a strong motivation for an inter-machine comparison of power width profiles, from which the correct size scaling should become evident.

As a second approach, we may use model 2B (parallel electron heat conduction + radial drift fluid velocity) directly, with a pre-factor determined based on a best fit to the JET empirical data. This method of estimating λ_q requires that we first fit the model 2B expression to the JET data, which yields the following expression,

$$\lambda_q \ [mm] = 1.1 * B[T]^{-7/11} \ q^{8/11} \ \varepsilon^{3/11} \ R[m]^{14/11} \ P[MW]^{-3/11} \ n[10^{19}m^{-3}]^{\ 7/11} \ A^0 \ Z^{1/22}$$

where $\varepsilon \sim 1/3$ and $R \sim 3$ m were used. Inserting the ITER values (with the same aspect ratio), one finds an ITER estimate of $\lambda_q \sim 5.5$ mm for all three species (the mass and charge dependence being negligible in model 2B). Once again, the validity of this best-fit expression requires validation on a multi-machine database.

CONCLUSIONS

In this article, we derived empirical scalings for inter-ELM and ELM wetted areas (power widths) versus engineering and plasma parameters. The key findings and their implications for ITER are summarized below:

(i) the previously reported narrow ($\sim$ 5 mm mapped to the outer mid-plane) inter-ELM heat load profiles on JET have been confirmed by high resolution IR thermography. The existence of such narrow profiles, typically only several ion gyro-radii in extent, imply the possibility of similarly narrow profiles on ITER.

(ii) the inter-ELM widths were found to be best matched by a model of SOL transport based on competition between parallel electron conduction and drift-ordered (Gyro-Bohm) perpendicular convection, model 2B in the notation of section 4, followed closely by marginal stability to interchange/ballooning modes, models 4a-c. If true, this would imply that radial transport in the near-SOL is dominated by residual levels of turbulence in the edge transport barrier, most likely driven by pressure gradient (resistive ballooning / interchange) instabilities.

(iii) the characterization of inter-ELM and ELM heat load profiles in ITER could be performed in both H and He plasmas and then extrapolated to D-T plasmas, correcting for the reported weak A and moderate Z dependence, i.e. since the mass and charge scaling exponents are very small, one can build up a reasonably accurate picture of D plasma SOL transport from examination of H and He plasmas. Moreover, it is fortunate that the power width exhibits a positive, although weak, Z scaling, so that power profiles are slightly broader in He than in D plasmas. This means that by starting with He plasmas, ITER would tackle the less challenging exhaust regime first, from which operational lessons could be learned.

14

(iv) the characterization of ELM impact factors may require H (as opposed to He) H-mode plasmas, due to the longer time scales of He ELM energy deposition and smaller degree of ELM profile broadening in He, compared to D and H, plasmas. While it would be possible to learn about ELM exhaust properties of D plasma based on He plasma observations, this would require good understanding of the underlying ELM exhaust processes, and hence, would introduce a degree of uncertainty in the prediction. On the other hand, such a step would carry operational benefits, since ELM heat loads in He plasmas would be smaller than in D plasmas, posing less risk to plasma facing components.

(v) Two techniques were used to predict the power width on ITER (direct extrapolation from equation (4) using the best fit mode 2B size scaling and extrapolation using model 2B), giving broadly similar results in the range of $\lambda_q \sim$ 5 - 7mm mapped to the outer mid-plane. This range is in good agreement with the standard ITER assumption (based on ballooning stability), i.e. the value assumed in the design of the ITER divertor, of $\lambda_q \sim$ 5mm, and indeed, with previous ITER predictions based on JET data ($\lambda_q \sim$ 4 - 5mm). The congruence between different estimates is likely coincidental since the dominant physics in model 2B is quite different to that in model 1A – 2A used for the previous extrapolation, and can perhaps be viewed as adding confidence to the ITER prediction. On the other hand, the weaker size scaling implied by several models which are consistent with JET D only data, e.g. model 1D+, lead to a possible downside risk of the ITER prediction, with possible values of λ_q as small as 3mm. The resolution of this dilemma should be possible following a multi-machine comparison of λ_q measurements, specifically a comparison between JET, AUG, D-IIID and Alcator C-mod tokamaks, all of which have the same aspect ratio, differ by only a factor of 2 in size and are equipped with good IR thermography cameras.

REFERENCES

[1.]   A. Chankin, presented at the 19th PSI Conference, San Diego, May, 2010; Journal of Nuclear Materials (2011) in press.

[2].   S. Devaux et al, presented at the 19th PSI Conference, San Diego, May, 2010.

[3].   T. Eich et al, Physics Review Letter (2003) T. Eich et al, Journal of Nuclear Materials (2005)

[4].   T. Eich et al, presented at the 19th PSI Conference, San Diego, May, 2010; Journal of Nuclear Materials (2011) in press.

[5]. T. Eich et al, in preparation for Plasma Physics and Controlled Fusion (2011).

[6]. W. Fundamenski et al, Plasma Physics Controlled Fusion, **48** (2006) 109-156.

[7]. W. Fundamenski, Fusion Science and Technology, **53** (2008) 1023-1063.

[8]. W. Fundamenski, Journal of Nuclear Materials, **390-391** (2009) 10-19.

[9]. W. Fundamenski, Power Exhaust in Fusion Plasmas, Cambridge University Press (2010).

[10]. E. Havlickova et al, Plasma Physics Controlled Fusion (2011), in press.

[11]. R.D. Hazletine and J.D. Meiss, Plasma Confinement, Addison-Wesley (1992).

[12]. P. Helander and D.J. Sigmar, Collisional Transport in Magnetized Plasmas, Cambridge University Press (2002).

[13]. S. Jachmich et al, presented at the 19th PSI Conference, San Diego, May, 2010.

[14]. B. LaBombard, Nuclear Fusion, (2005).

[15]. G. Kirnev, Plasma Physics and Controlled Fusion (2005)

[16]. R.A. Pitts et al, Nuclear Fusion (2005)

[17]. Presented at the 19th PSI Conference, San Diego, May, 2010; Journal of Nuclear Materials (2011) in press.

[18]. D. Tskhakaya et al, Contributions to Plasma Physics, **46** (2006) 649.

JET Pulse No.	t	A	Z	B	Ip	$\langle n \rangle$	P	ε	$E_{ELM.5}$	η	τ	W_{dia}	A_w ELM	A_w i-ELM
73920	25	2	1	1.1	1	2.6	6	12	8.5	205	0.003	1.17	0.72	0.55
73920	31	2	1	1.1	1	2.4	5	13	10.5	211	0.003	1.22	0.84	0.52
79215	22	4	2	1.1	1.1	2.9	5	13	17	190	0.004	0.82	1.08	0.62
79215	27	4	2	1.1	1.1	3.1	7.1	9.2	14	176	0.004	0.85	1	0.95
79283	21	1	1	1.1	1	2.3	3	4	0.3	110	0.004	0.69	0.95	0.5
79283	23	1	1	1.1	1	3	6	14	0.7	289	0.002	0.89	1.1	0.6
79283	26	1	1	1.1	1	3.25	2.8	15	3.5	150	0.093	0.69	1	0.95
73660	21	2	1	1.58	1.5	4.5	4.2	35	35	600	0.003	1.9	1.07	0.51
73660	23	2	1	1.58	1.5	4.3	7.2	33	36	600	0.003	2.3	1.13	0.55
73660	25	2	1	1.58	1.5	3.7	13	18	22.5	400	0.002	2.86	1.1	0.6
79140	24	4	2	1.5	1.45	3.4	6	34	40	300	0.028	1.15	1	0.64
79390		1	1	1.5	1.48	3.2	6	25	23	145	0.002	1.6	1	0.51
79390		1	1	1.5	1.48	3.2	11	24	23	475	0.002	1.8	1	0.48
74391	22	2	1	2	2	11.5	7.8	62	62	1380	0.002	6.8	0.95	0.43
79373	22	1	1	2	2	4.5	12	26	31	821	0.002	2.96	0.85	0.53
76481	20	2	1	2	2	5.5	11	34	33.7	800	0.007	4.01	1	0.47
79214	21	4	2	2.5	2.5	4.4	10	44	23.8	390	0.009	2.66	0.65	0.48
77557	20	2	1	2	2	5	16	19	15.9	510	0.002	3.91	0.76	0.4
79756	24	2	1	1.5	1.5	4	10	33	33.8	700	0.002	2.69	1.12	0.52
79211		4	2	1.5	1.5	4.3	10	23	25.6	360	0.004	1.42	1.12	0.62
79755		2	1	2	1.5	3.5	10	31	37.8	670	0.002	2.59	1.2	0.62
79141	24	4	2	2.25	1.5	3.2	9.4	26	44.7	270	0.007	1.44	0.95	0.67
74373	19	2	1	2.45	2.5	6.46	18	61	70.2	1140		6.37	1.35	0.45
74376	20	2	1	2.45	2.5	6.8	15	42	46.7	760		5.89	1.28	0.47

Table 1: Summary of experimental data resulting from the present experiment. The rows indicate (~ 1 sec) time windows in distinct discharges during which data was collected. The columns list relevant quantities (units given below in brackets): fuel ion mass number, $A = m_i/m_p$, and charge number, $Z = e_i/e$, toroidal field on axis, B [T], plasma current, I_p [MA], line average electron density, $\langle n \rangle$ [$10^{19} m^{-3}$], heating power, P_H[MW], maximum ELM energy load, ε [kJ/m2], mean ELM energy load on the outer target load bearing tile (tile 5), $E_{ELM,5}$ [kJ], ELM impact factor, η [$kJ/m^2 s^{1/2}$], mean temporal width of the ELM heat pulse at the divertor target, τ [s], plasma diamagnetic energy, W_{dia} [MJ], ELM wetted area on tile 5, A_w^{ELM} [m^2], and inter-ELM wetted area on tile 5, A_w^{i-ELM} [m^2].
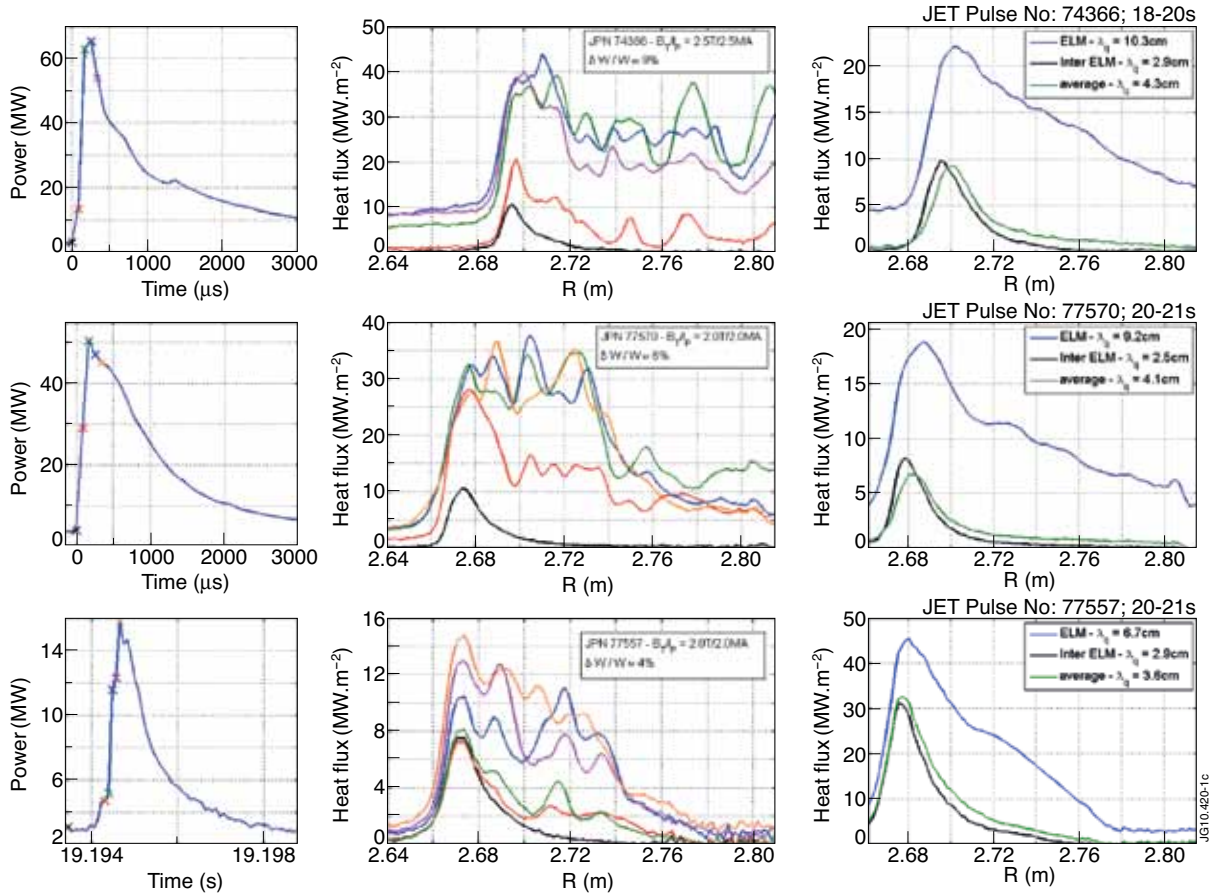
Figure 1: Radial heat load profiles on the outer divertor target for three distinct deuterium discharges with different mean relative ELM size (W_{ELM}/W_{dia}): 9% (top), 6% (middle), 4% (bottom). The left frames show the temporal evolution of the power arriving at the target during the ELM crash. The middle frames show a series of snapshots of the heat load profiles during the course of the ELM crash (as indicated on the left frames). The right frames show radial heat load profiles during the inter-ELM and ELM peak phases, time-averaged over 1-2 s, along with average total heat load profile during the same time.
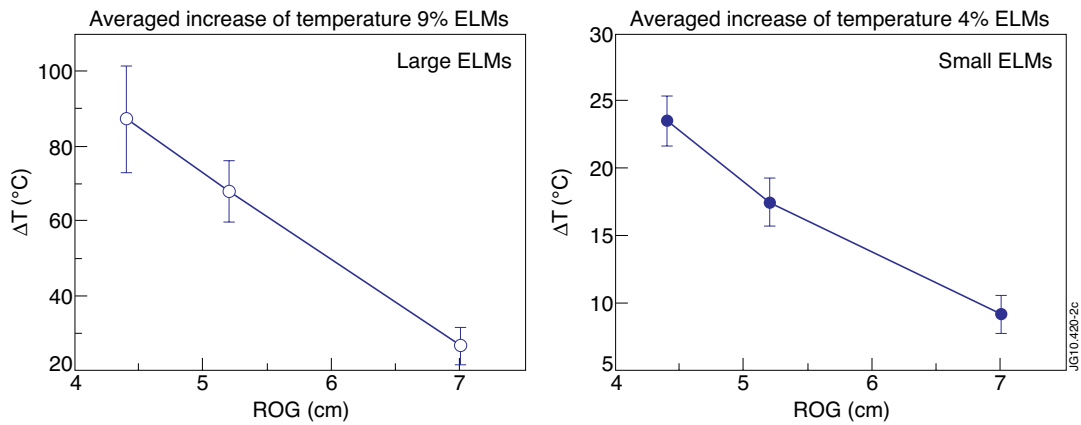
Figure 2: ELM heat load interaction with outer limiter for two D discharges, with relative ELM size, (W_{ELM}/W_{dia}) of 9% (left) and 4% (right), for different values of the outer gap (ROG)
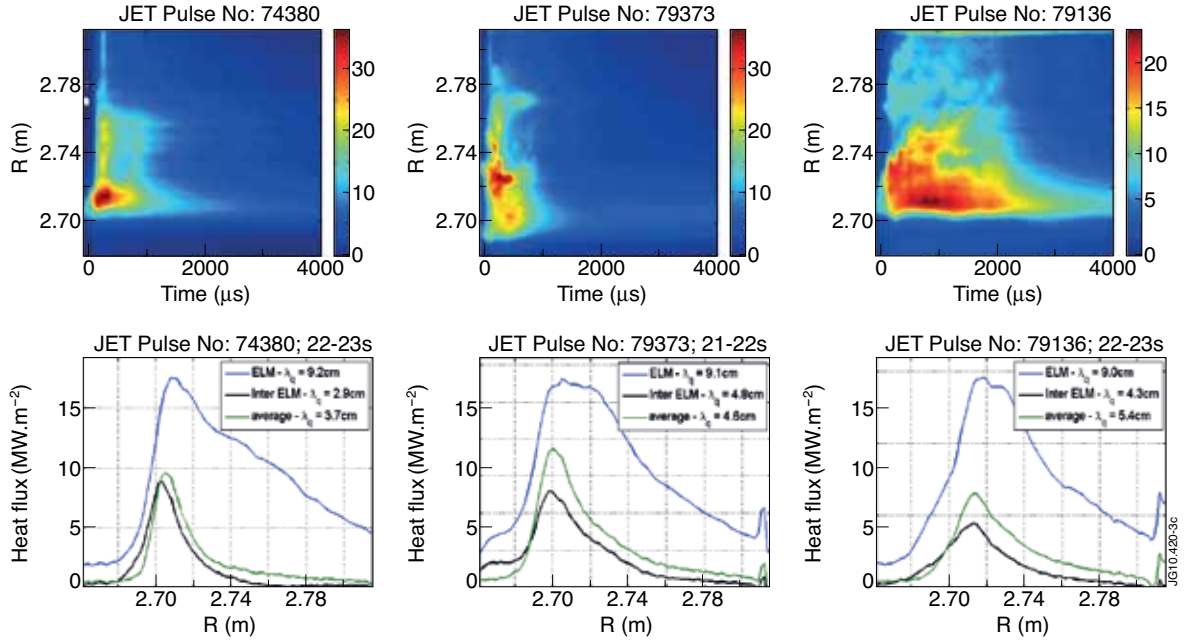
Figure 3: Radial heat load profiles on the outer divertor target in comparable D, H and He plasmas. The bottom frames show inter-ELM, ELM and average profiles and their corresponding integral widths. The top frames show the temporal evolution of the heat load profiles during a typical, medium sized ELMs ($W_{ELM}/W_{dia} \sim 4\text{-}5\%$).
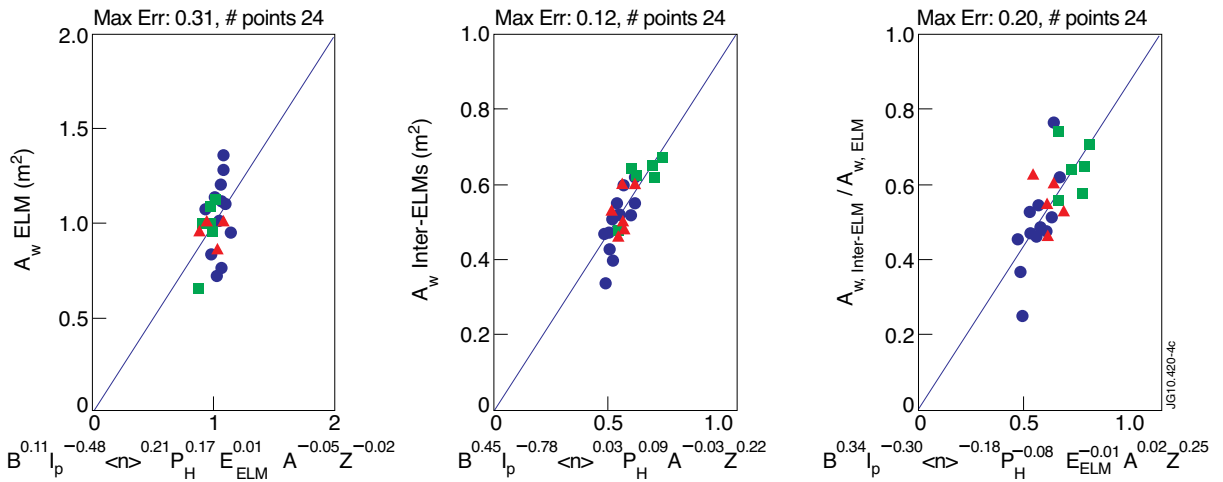

Figure 4: IR-measured wetted areas, A_W [m^2], during ELM (left), inter-ELM (middle) and their ratio (right) vs best-fit scalings with field, current, density, heating power, A and Z (and for ELM quantities also with ELM deposited energy) for all ion species.
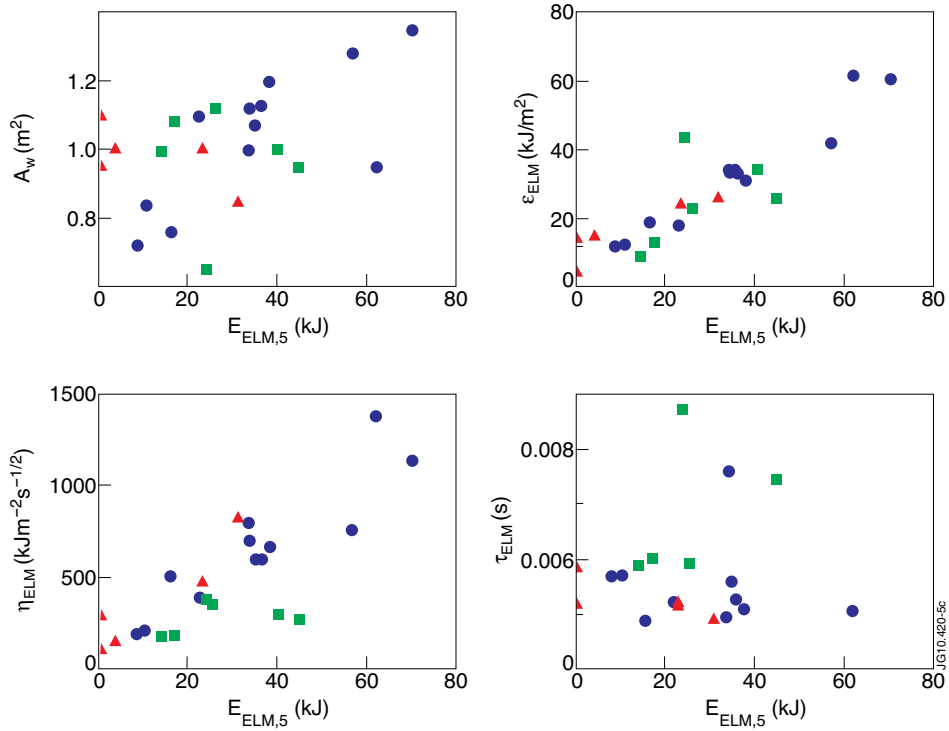
Figure 5: ELM wetted area (top left), ELM energy load (top right) and ELM impact factor (bottom left) and ELM deposition time scale (bottom right) versus ELM deposited energy (kJ).
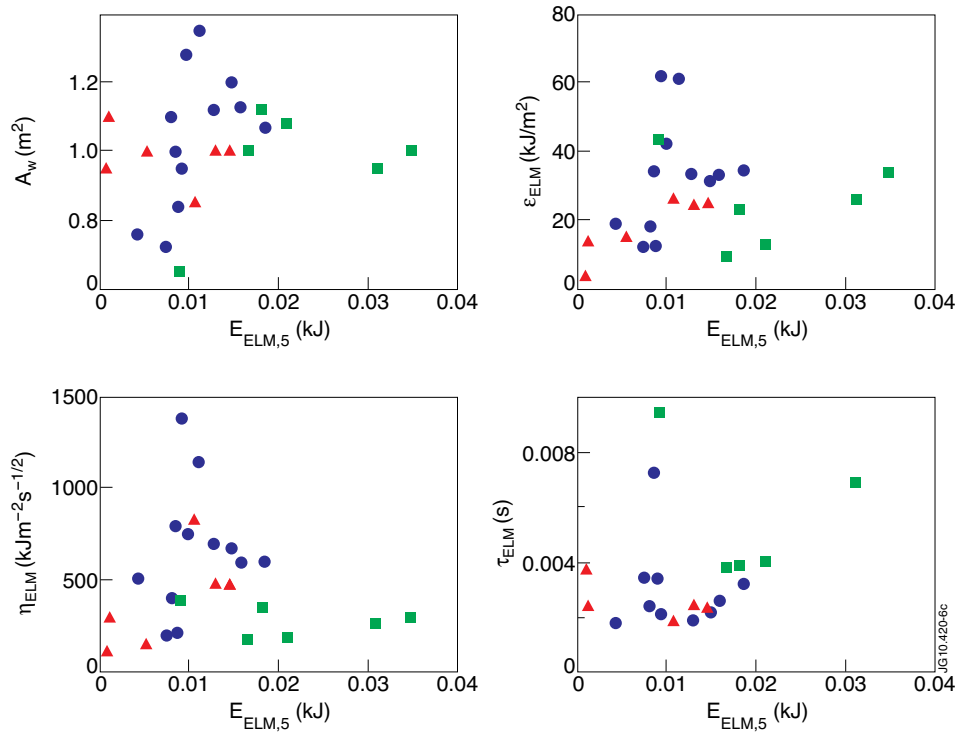
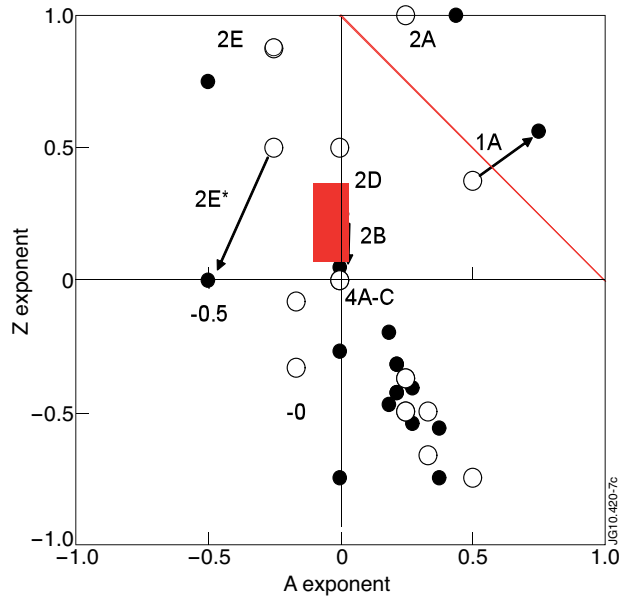*Figure 6: Same as Figure 6, but plotted versus normalized ELM deposited energy.*

Figure 7: Comparison of model predictions with the inferred A and Z scaling for the inter-ELM phase of JET discharges (open circles = model scalings at constant SOL temperature, solid circles = model scalings at constant SOL power, red/grey region = experimental result, rough extent of error bars).
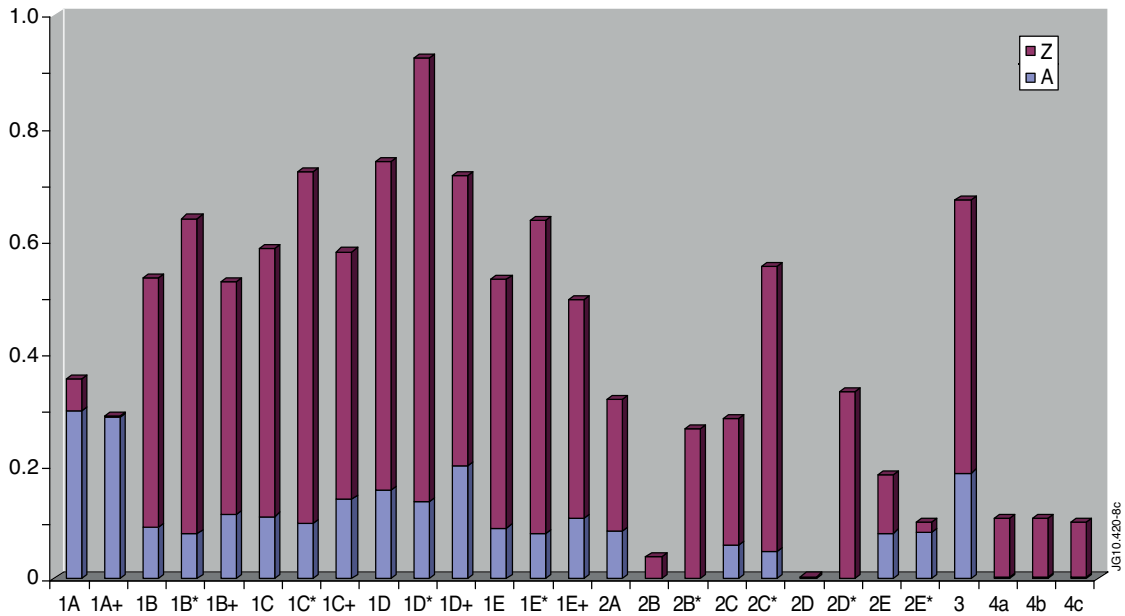

Figure 8: Root mean square errors between predicted and inferred (based on models described in the text) scaling exponents for the heat load power width with A and Z in the inter-ELM phase of JET discharges (same data as in Figure 8). Experimental RMS error bar (uncertainty level) on the exponents ~ 0.13.
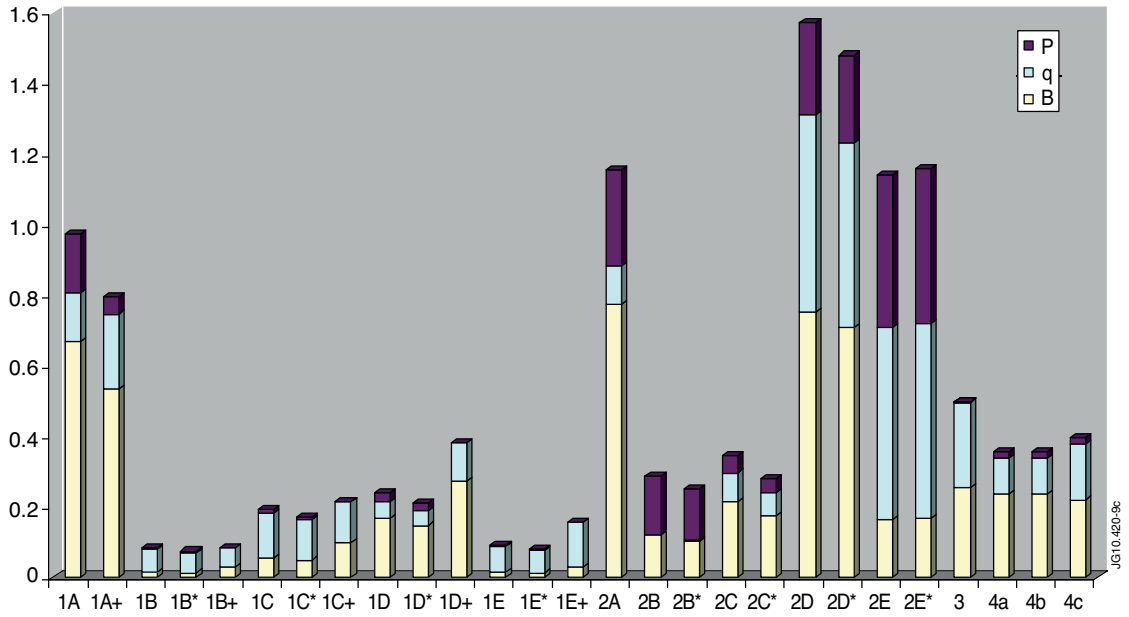
Figure 9: Root mean square errors between predicted and inferred (based on models described in the text) scaling exponents for the heat load power width with P, q, B. Experimental RMS error bar (uncertainty level) on the exponents ~ 0.25. (excluding the A & Z dependence) in the inter-ELM phase of JET discharges (complimentary to Figure 8).
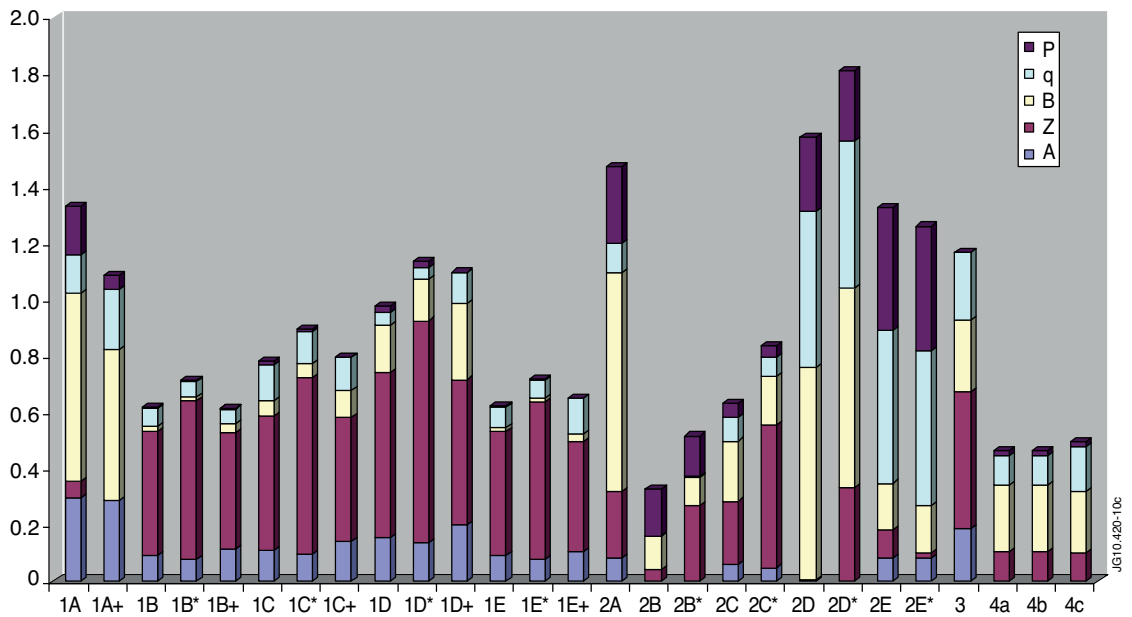

Figure 10: Root mean square errors between predicted and inferred (based on models described in the text) scaling exponents for the heat load power width with n, P, q, B, Z and A in the inter-ELM phase of JET discharges. Experimental RMS error bar (uncertainty level) on the exponents ~ 0.25.